

Measurement of the energy-differential $^{35}\text{Cl}(n, p_0)^{35}\text{S}$ cross section via the ratio with $^6\text{Li}(n, \alpha)^3\text{H}$

T. S. Nagel,^{1,*} J. A. Brown,¹ J. C. Batchelder,¹ D. Bleuel,² C. A. Brand,^{1,2} A. Georgiadou,¹ B. L. Goldblum,^{1,3} M. Fratoni,¹ J. M. Gordon,¹ T. A. Laplace,¹ and L. A. Bernstein,^{1,3}

¹*Department of Nuclear Engineering, University of California, Berkeley, California 94720, USA*

²*Lawrence Livermore National Laboratory, Livermore, California 94550, USA*

³*Lawrence Berkeley National Laboratory, Berkeley, California 94720, USA*



(Received 30 March 2024; accepted 1 August 2024; published 12 September 2024)

Background: Knowledge of the neutron-induced $^{35}\text{Cl}(n, x)$ cross sections is vital to the design and certification of molten chloride fast reactors (MCFRs) since the $^{35}\text{Cl}(n, p_0)^{35}\text{S}$ reaction is believed to be a significant reactor poison. However, recently published measurements are inconsistent with each other and with evaluation.

Purpose: The goal of this work is to measure the $^{35}\text{Cl}(n, p_0)$ reaction cross section using a technique that is different from recent measurements.

Methods: The experiment was conducted at Lawrence Berkeley National Laboratory's (LBNL) 88-Inch Cyclotron using thick target deuteron breakup from a 14 MeV deuteron beam. Energy-differential $^{35}\text{Cl}(n, p_0)^{35}\text{S}$ cross sections were obtained via ratio with the $^6\text{Li}(n, \alpha)^3\text{H}$ reaction using an active target experiment with a $\text{Cs}_2\text{LiYCl}_6$ (CLYC) scintillator.

Results: The $^{35}\text{Cl}(n, p_0)$ reaction cross section was measured from 2.02 to 7.46 MeV. The results are consistent with Kuvin *et al.*, confirming a roughly 50% reduction in magnitude relative to the ENDF/B-VIII.0 evaluation.

Conclusions: These data provide new insight into the role of natural Cl as an MCFR poison. The reduction of the $^{35}\text{Cl}(n, p_0)$ reaction cross section compared to evaluation suggests that MCFR criticality is less sensitive to Cl enrichment. This may in turn reduce building and operating costs since isotope separation may not be needed.

DOI: [10.1103/PhysRevC.110.034612](https://doi.org/10.1103/PhysRevC.110.034612)

I. INTRODUCTION

Many modern, advanced reactor designs strive to increase efficiency, safety, and reliability, while simultaneously decreasing proliferation risk and radioactive waste by exploring exotic fuels and coolants. One such reactor type is the molten chloride fast reactor (MCFR). The MCFR is a fast spectrum reactor in which molten fuel is mixed with a chlorine-based salt, forming a salt-fuel eutectic which acts as both the fuel and the primary coolant [1]. In addition to the preeminent importance of the (n, p) channel to the MCFR neutron economy, the low mass and limited valence nucleon number of the $n + ^{35}\text{Cl}$ system makes it challenging to model. It is well above the region typically described by the α -cluster model and has too many valence particles for easy treatment by the independent particle shell model, but it still lacks sufficient level density to completely justify the use of statistical reaction modeling using the Hauser-Feshbach formalism. This is evident in the recent measurements by Batchelder [2] *et al.* and Kuvin *et al.* [3], both of which show broad, resonant-like behavior at MeV energies. Additionally, the Nuclear Energy Agency has included the $^{35}\text{Cl}(n, p)$ reaction on its “Nuclear Data High Priority Request List” [4]. This work, which measured the $^{35}\text{Cl}(n, p_0)$ cross section relative to the well-known $^6\text{Li}(n, \alpha)^3\text{H}$ channel, provides guidance for the nuclear data

evaluation community on how to best address reaction modeling in this intermediate mass region, information that is relevant not only to reactor design, but also to neutron active interrogation and even the to start of neutron-driven astrophysical nucleosynthesis.

The current state of evaluated nuclear data [5] suggests that neutron loss through (n, p) , (n, γ) , and (n, α) on ^{35}Cl is significant in the MCFR energy range. This loss negatively impacts core reactivity. Additionally, the production of long-lived ^{36}Cl ($t_{1/2} = 301 \pm 15$ kyr) via (n, γ) is undesirable from a waste management perspective [6]. On the other hand, ^{37}Cl has little to no (n, p) , (n, γ) or (n, α) cross section in this energy range. Unfortunately, natural chlorine is about 75% ^{35}Cl and 25% ^{37}Cl . Enrichment of the chlorine in ^{37}Cl would mitigate these concerns but at a potentially large expense [1]. For neutron energies above approximately 200 keV, only two experimental measurements of the $^{35}\text{Cl}(n, p)^{35}\text{S}$ cross section are available.¹ Both of these measurements, Batchelder *et al.* [2] and Kuvin *et al.* [3], indicate a significantly reduced magnitude of the $^{35}\text{Cl}(n, p)$ cross section compared to the ENDF/B-VIII.0 values.

¹A third measurement in the form of a Master's thesis is available [7]. This work was a CLYC measurement but done absolutely (i.e., not in ratio).

*Contact author: TNagel@lbl.gov

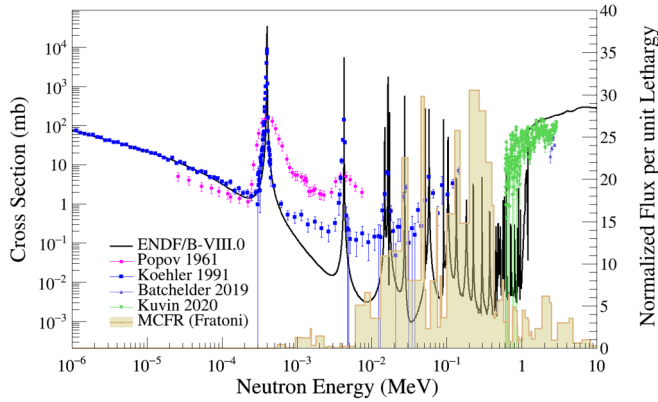


FIG. 1. Experimental measurements and ENDF/B-VIII.0 evaluation of the $^{35}\text{Cl}(n, p)^{35}\text{S}$ cross section on the primary axis. The secondary axis provides the normalized MCFR neutron flux per unit lethargy [6].

Batchelder *et al.* [2] measured the energy-integrated $^{35}\text{Cl}(n, p)$ and $^{35}\text{Cl}(n, \alpha)$ cross sections from 2.42 to 2.74 MeV using activation. Neutrons with an energy range of 2.18–2.74 MeV were produced via deuterium-deuterium (DD) fusion neutrons using the High Flux Neutron Generator [8] at the University of California, Berkeley. A series of NaCl pellets, coloaded with natural Ni foils, were placed at various angles with respect to the beam. The $^{35}\text{Cl}(n, p)^{35}\text{S}$ and $^{35}\text{Cl}(n, \alpha)^{32}\text{P}$ cross sections were determined relative to the reference $^{58}\text{Ni}(n, p)^{58}\text{Co}$ cross section. Their results for the (n, α) cross section agreed well with the evaluated data libraries, but the (n, p) values were a factor of 3 to 5 times lower than the evaluated libraries. The experimental values were not only much lower than expected but showed a clear resonance structure, indicating a resolved resonance model rather than a statistical Hauser-Feshbach model is more appropriate in this energy range.

Kuvin *et al.* [3] performed measurements of the partial, energy-differential (n, p_i) and (n, α_i) cross sections from 0.6 to 6 MeV and used a different experimental technique. In this experiment, neutrons from the WNR spallation source [9] at Los Alamos National Laboratory (LANL) were directed to a NaCl target and charged particles produced were measured using the Low Energy (n, z) (LENZ) system. Their work confirms the large overestimation of the (n, p) cross section in evaluated libraries as well as a resonance behavior up to 3 MeV.

Figure 1 shows the evaluated ENDF/B-VIII.0 $^{35}\text{Cl}(n, p)^{35}\text{S}$ cross section [5] along with four previous measurements: Batchelder [2], Kuvin [3], Koehler [10], and Popov [11]. The yellow histogram represents a modeled MCFR neutron flux in normalized flux per unit lethargy [6]. The figure shows a clear lack of experimental data in the region where the MCFR flux peaks. The two recent experiments, Batchelder and Kuvin, agree with a reduction in the magnitude compared to ENDF, but disagree in their absolute magnitudes. This discrepancy is highlighted in Fig. 2, where the Batchelder *et al.* data are seen to be roughly half those of Kuvin *et al.*

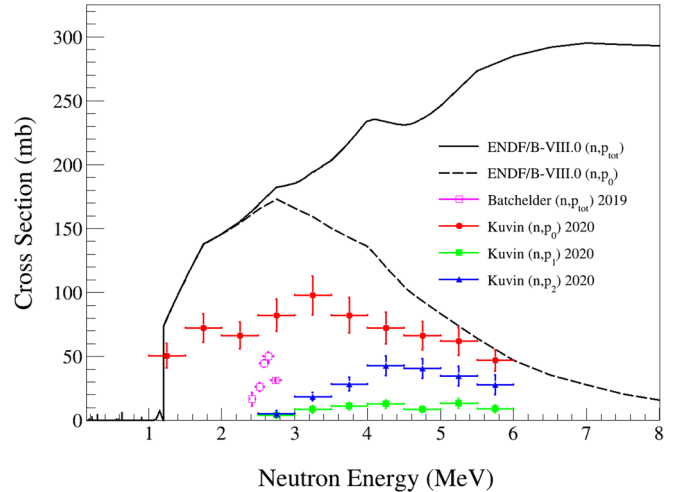


FIG. 2. The $^{35}\text{Cl}(n, p)^{35}\text{S}$ cross section, highlighting the inconsistency of existing experimental data.

To help adjudicate these discrepancies, the $^{35}\text{Cl}(n, p_0)^{35}\text{S}$ cross section was measured in the energy range of 2.02 to 7.46 MeV. Section II describes the experimental setup, neutron source, and data acquisition. Section III describes the data analysis and presents the results. Section IV is a summary.

II. EXPERIMENT

The development of neutron-sensitive elpasolite scintillators containing chlorine [e.g., $\text{Cs}_2\text{LiYCl}_6$ (CLYC)] allow for active target measurements of $\text{Cl}(n, x)$ cross sections. CLYC has been rising in popularity due to its triple-mode use (fast neutron, slow neutron, and gamma) along with relatively high γ -ray energy resolution and good sensitivity to fast and slow neutrons [12–16]. Neutron sensitivity in CLYC comes from several reactions. These include $^6\text{Li}(n, \alpha)^3\text{H}$, $^{35}\text{Cl}(n, p)$, and $^{35}\text{Cl}(n, \alpha)$. Our technique, which determines the $^{35}\text{Cl}(n, p_0)^{35}\text{S}$ cross section in ratio to the $^6\text{Li}(n, \alpha)^3\text{H}$ reaction, is distinct from and complementary to other measurements.

A. Experimental setup

The experiment was performed at the 88-Inch Cyclotron at Lawrence Berkeley National Laboratory (LBNL) [17]. Figure 3 is a sketch of a portion of the 88-Inch Cyclotron laboratory. On the right side of the figure is the cyclotron vault, which contains the cyclotron itself, the breakup target, and a beam collimator. On the left side is the Cave 5 experimental area which contains the active target scintillator. The two rooms are separated by a 2.44-m-thick wall made of concrete and steel. A 10-cm-diameter steel beampipe allows for neutrons produced in the vault to enter Cave 5. A broad energy neutron beam is produced in the vault via thick target deuteron breakup (TTDB) using a 14 MeV deuteron beam and graphite breakup target. The resulting neutron beam is immediately impinging on a 60-cm-long copper collimator resulting in a neutron beam width of approximately 12 cm in the experimental area. The neutron beam is then passed through an

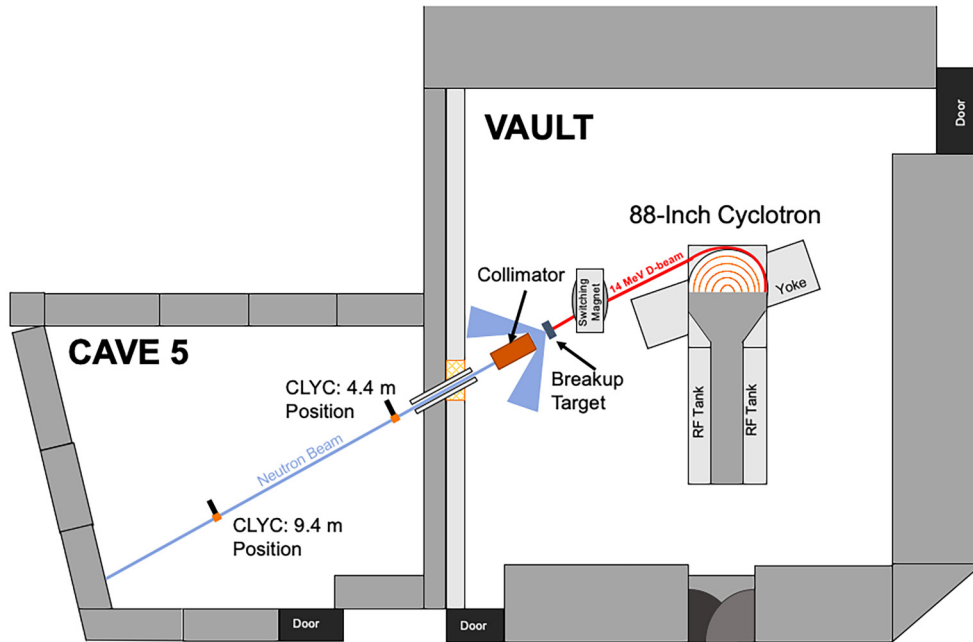


FIG. 3. Sketch of a portion of the Berkeley 88-Inch cyclotron experimental facility. A collimated neutron beam was produced via breakup of 14 MeV deuterons on a thick graphite target. The CLYC active target scintillator was placed at two different locations within the cave: 4.4 m and 9.4 m. Image is not drawn to scale.

air-filled beampipe into Cave 5 where it arrives at the CLYC detector. This experiment used a 25-mm-diam. \times 25-mm-high right circular cylindrical CLYC6 scintillator (i.e., enriched in the ${}^6\text{Li}$ isotope to 95%) from Radiation Monitoring Devices [18] as an active target. Enrichment in ${}^6\text{Li}$ was chosen to enhance the ${}^6\text{Li}(n, \alpha){}^3\text{H}$ signal. In this work, measurements were made at two different flight path lengths, a 9.4 m long flight path and a 4.4 m short flight path. The two cases constitute independent data sets. The scintillator crystal was mounted to a 51-mm-diam. Hamamatsu H13795-100-Y002 photomultiplier tube [19] with a 1-mm-thick Eljen EJ-560 silicon optical coupling pad [20]. The detector assembly was placed on a tripod to facilitate ease of movement between the two positions as well as alignment in the beam. The detector assembly was placed at a right angle to the beam with the scintillator crystal directly in the beam; this geometry kept the photomultiplier tube largely out of the beam. The detector was centered in the beam by aligning a Huepar 902CG cross line laser level [21] with predetermined beamline reference points on the cave walls.

B. Neutron source

For this experiment, ${}^2\text{H}^+$ ions were accelerated to 14 MeV for the entirety of data collection. Beam current was 100 nA for the 4.4 m and 300 nA for the 9.4 m data set. For our case of 14 MeV deuterons, the radio frequency (RF) was 5.907 MHz, corresponding to a pulse period of 169.3 ns. The beam had a temporal width of 8.5 ns sigma for the 4.4 m and 6.0 ns sigma for the 9.4 m data set.

Upon exiting the cyclotron the 14 MeV deuterons were impinged on a 3.5-mm-thick graphite breakup target creating

a neutron beam via thick target deuteron breakup. The target is sufficiently thick to stop all secondary reaction protons. The resulting neutron spectrum was roughly Gaussian with a median energy of 6 MeV and a full width at half maximum (FWHM) of 7 MeV [22]. Frame overlap, also called wraparound [23], is a neutron energy ambiguity phenomenon that results from using a neutron spectrum that is both broad in energy and cyclic in time. Since each pulse contains neutrons with a wide variation in energy, fast (high energy) neutrons from one pulse can arrive at a given location at the same time relative to the repeated RF signal from the cyclotron as slow (low energy) neutrons from a previous pulse. This introduces an ambiguity in the time of flight (TOF). The point at which this overlap occurs depends on the flight path length and pulsing period.

C. Data acquisition

Data acquisition (DAQ) was performed with a CAEN DT5725S desktop digitizer [24] with Digital Pulse Processing–Pulse Shape Discrimination firmware [25]. Analog-to-digital conversion was via a 14-bit, 250-MS/s flash ADC. CAEN’s multiparametric software, COMPASS [26], was used to set parameters and record data for the experiment. Relevant acquisition parameters are listed in Appendix A. Leading edge triggering was adopted to mitigate bias due to shape differences observed in the neutron- and gamma-induced signals [27]. Timing synchronization with the cyclotron was accomplished by recording the cyclotron RF control signal. CLYC-RF coincidences were built during postprocessing. The digitizer FPGA provides long and short charge integrals (Q_{long} , Q_{short}) which were used to form a

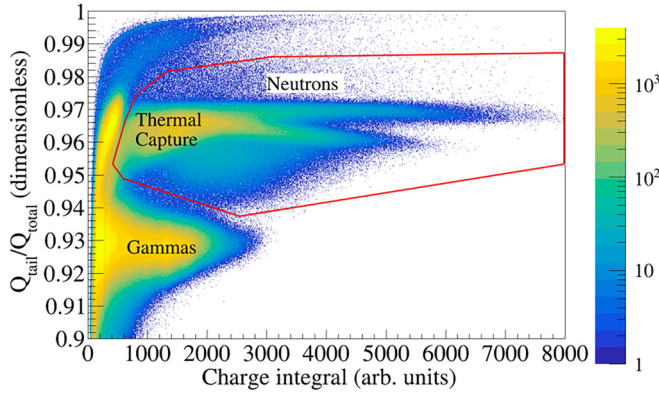


FIG. 4. Pulse shape discrimination metric as a function of total charge in CLYC.

tail-to-total pulse shape discrimination (PSD) metric:

$$\text{PSD} = \frac{Q_{\text{tail}}}{Q_{\text{total}}}, \quad (1)$$

where $Q_{\text{tail}} = Q_{\text{long}} - Q_{\text{short}}$ and $Q_{\text{total}} \equiv Q_{\text{long}}$. A representative PSD plot is shown in Fig. 4. Neutron pulses, having proportionally more delayed light than equivalent-energy γ -ray pulses, have a larger value of PSD and correspond to the top band in the figure, whereas γ -ray pulses correspond to the lower band. The artifact present at small charge integral values is due to the system re-triggering on the tail of the pulse. A graphical cut, represented by the red line, was used to select neutron induced reactions.

III. ANALYSIS

A. Timing calibrations

Incident neutron energy was determined using a TOF technique. Frame overlap necessitates a relative instead of absolute timing scheme. For each event, a “time-since-last-RF” was calculated:

$$\Delta t_{\text{event}} = t_{\text{RF}} - t_{\text{event}}, \quad (2)$$

where t_{event} is the scintillator timestamp and t_{RF} is the cyclotron RF timestamp. Neutron events are converted from “time since last RF” to TOF by adding a calibration constant that represents the difference between the γ -ray TOF and the measured Δt_{γ} . The neutron time of flight is given by

$$\text{TOF}_n = \Delta t_n - \Delta t_{\gamma} + L/c, \quad (3)$$

where TOF_n is the neutron TOF, Δt_{γ} is the measured γ -ray time relative to the RF, and L/c is the γ -ray TOF.

Variation in the signal time as function of signal pulse height (i.e., time trigger walk) as a result of leading edge triggering, was observed for events with small light yield values. Over the light yield ranges of interest, the time of flight was seen to walk by 1 ns, resulting in a neutron energy walk of 1%. The different pulse shapes between neutron and gamma events can produce another type of timing error resulting from their differing rise times. This effect was recently reported by [27] who observed a time bias values of 2–4 ns when using a constant fraction discrimination (CFD) setup. We investigated

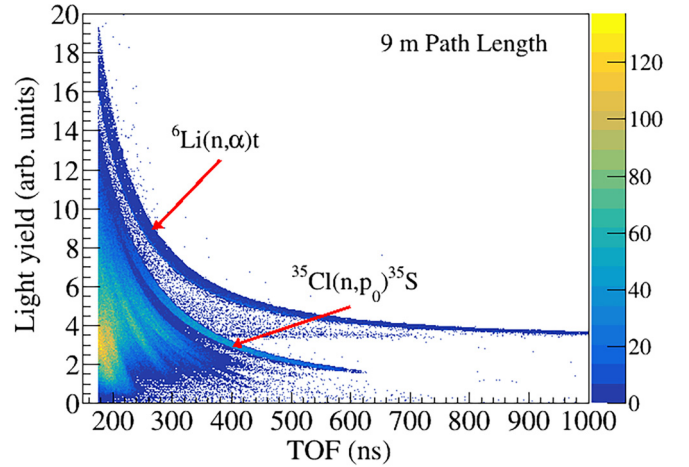


FIG. 5. GEANT4 simulation showing the various kinematic bands. The desired ${}^6\text{Li}(n, \alpha){}^3\text{H}$ and ${}^{35}\text{Cl}(n, p){}^{35}\text{S}$ bands are well separated.

this potential timing bias by calculating the time trigger offset between γ -ray and neutron pulses for our leading edge discrimination setup. For all pulse heights and reaction channels used in this work, it was observed to be negligible.

B. Monte Carlo modeling

The detector response to neutrons was simulated using the GEANT4 software package [28] to guide interpretation of the experimental data. A 2.54 cm by 2.54 cm, square, parallel, uniform neutron source from 0.05 to 14 MeV was directed to the side of the scintillator crystal. The simulations were performed at two distances: 4 and 9 m. Neutrons incident on CLYC can undergo many reactions, each of which produces a characteristic kinematic band. The amount of scintillation light produced for a given reaction is a function of the neutron energy, the reaction Q value, and the reaction product particle type. The light output vs neutron energy results for the 9 m model are shown in Fig. 5. An imperfect light yield calibration was used, hence the continued use of arbitrary units. A number of features are visible. First, the energetic ${}^6\text{Li}(n, \alpha){}^3\text{H}$ reaction, ($Q_{n,\alpha} = 4783$ keV), produces a well separated band with a large light yield. Second, the smaller- Q -value reaction ${}^{35}\text{Cl}(n, p_0)$ ($Q_{n,p} = 615$ keV) produces a bright band at a lower light yield. Third, ${}^{35}\text{Cl}(n, p\gamma)$ bands are significant and appear below the (n, p_0) band. Fourth, all other reactions including those on ${}^{37}\text{Cl}$ and ${}^7\text{Li}$ are minimal and tend to lie on top of one another below the (n, p_0) band. This also implies that direct measurements of ${}^{35}\text{Cl}(n, p\gamma)$ and ${}^{35}\text{Cl}(n, \alpha)$ cross sections may not be possible. Lastly, a significant amount of downscatter is seen in the ${}^6\text{Li}(n, \alpha){}^3\text{H}$ reaction. In the experimental case, these bands do not continue uninterrupted to arbitrarily long TOF as shown in Fig. 5, but instead will “wrap” over the previous data at some point. This “wrap point” is dependent on the flight path length. Figures 6 and 7 show the GEANT4 simulations in which the output has been wrapped for two different path lengths. For a path length of 9 m the wrap point occurs at an energy of 3.5 MeV and for a 4 m path length it occurs at 1.3 MeV. Thus, by utilizing two different path lengths the unwrapped energy

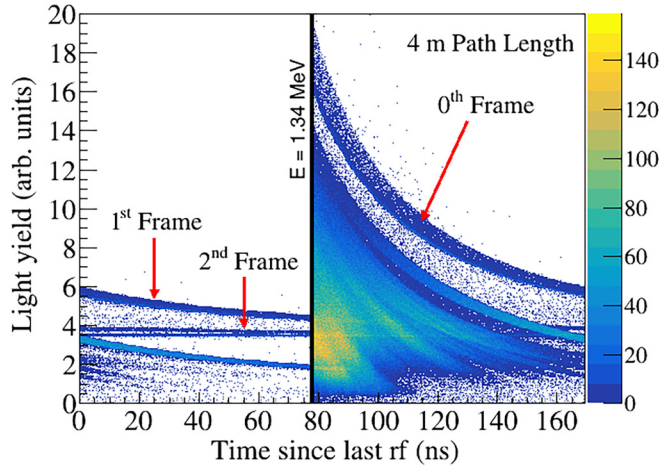


FIG. 6. Wrapped GEANT4 simulation for a path length of 4 m with a wrap point at 1.34 MeV.

range is maximized. Due to space constraints within the cave the experimental detector locations were 9.4 and 4.4 m.

C. Experimental $^{35}\text{Cl}(n, p_0)$ cross section

Figures 8 and 9 show the experimental integrated charge vs time-of-flight neutron-gated data for path lengths of 4.4 and 9.4 m respectively. For clarity, two periods are shown. Viewed in this way, the kinematic bands can be seen to continue from one frame to the next. This is equivalent to the picture in which a band exits the figure on the right side and then reappears on the left side. The experimental band structure is similar to that seen in the GEANT4 model with the addition of experimental resolution. The zeroth frame of the energetic $^6\text{Li}(n, \alpha)^3\text{H}$ band is at the top of the figure. Subsequent frames are hidden by the emergence of lower- Q -value reactions but they eventually reappear as a horizontal band. This represents the minimum possible light yield from the reaction and is likely due to the 240 keV resonance in the reaction as well as any signal from residual thermal and room

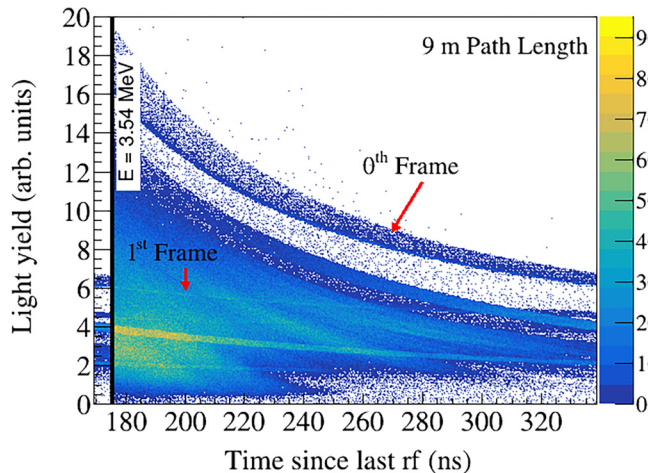


FIG. 7. Wrapped GEANT4 simulation for a path length of 9 m with a wrap point at 3.54 MeV.

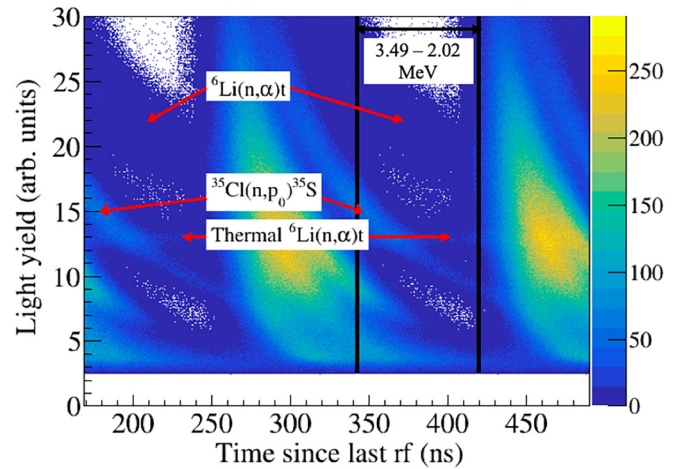


FIG. 8. Various kinematic reaction bands for a path length of 4.4 m. Data were gated on neutron events.

return neutrons (inherently time independent due to their long birth time relative to the cyclotron period). A 240 keV neutron has a TOF of 650 ns for a 4.4 m flight path (1387 ns for 9.4 m) which corresponds to 3.8 RF periods. As can be seen from the model in Fig. 6, the band is nearly flat after just two wraps. Thus, by the time the band has reached 240 keV it is, within the light resolution of the detector, perfectly flat. This band is considered perfectly time independent. The $^6\text{Li}(n, \alpha)^3\text{H}$ band is unique in that it produces two light-producing particles which are emitted back to back in the center-of-mass (CoM) frame. They have the following kinematic relationship:

$$T_\alpha = \frac{Q}{1 + m_\alpha/m_t}, \quad (4)$$

where T_α is the α -particle kinetic energy, m_α and m_t are the particle masses, and Q is the reaction Q value. The kinetic energy for the particle is thus $(3/7)Q$ while for the triton it is $(4/7)Q$. The α particle, having twice the nuclear charge of the triton, will be more quenched since quenching is correlated to dE/dx [29]. Since both particles are always present with some

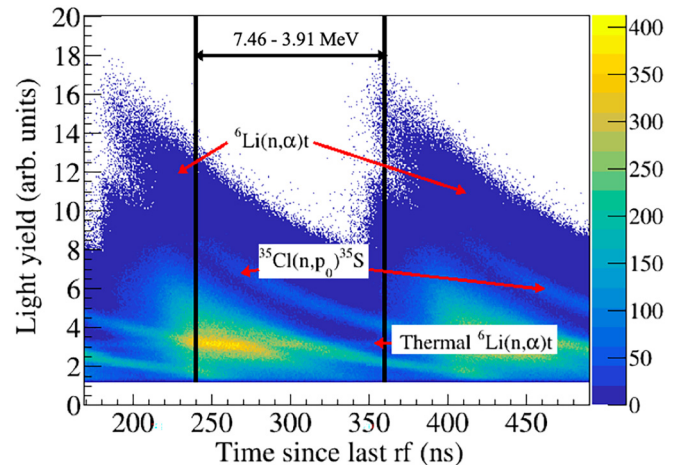


FIG. 9. Various kinematic reaction bands for a path length of 9.4 m. Data were gated on neutron events.

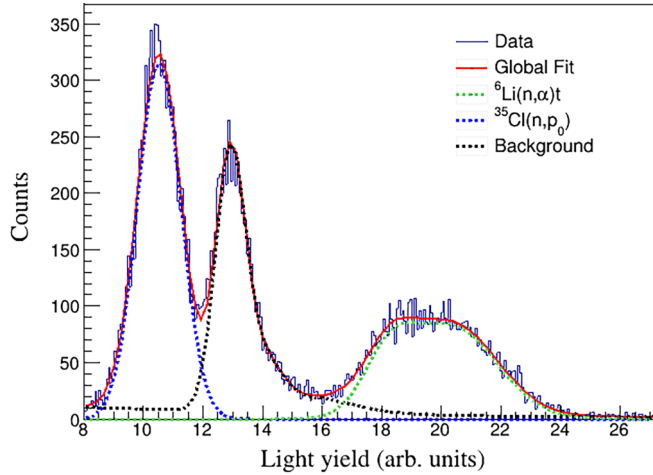


FIG. 10. Representative fit for 4.4 m data set at 2.02 MeV.

energy and since the particles are emitted isotropically in the CoM, the exact energy sharing depends on the emission angle with respect to the CoM direction. This causes the ${}^6\text{Li}(n, \alpha)$ reaction band to exhibit a broad bimodal distribution that is more pronounced at higher incident neutron energies (short TOF). Conversely, the ${}^{35}\text{Cl}(n, p_0)$ band, which has only one light producing particle, appears as a single narrow band and is located beneath the Li band due to its lower Q value. Even with an unknown amount of quenching, assignment of the ${}^{35}\text{Cl}(n, p_0)$ and ${}^6\text{Li}(n, \alpha)$ ${}^3\text{H}$ bands is unambiguous since the ${}^{35}\text{Cl}(n, p_0)$ band is seen to extend below the horizontal minimum energy ${}^6\text{Li}(n, \alpha)$ ${}^3\text{H}$ band in Fig. 8.

The determination of the ${}^{35}\text{Cl}(n, p_0)$ cross section in this work is done in ratio to the ${}^6\text{Li}(n, \alpha)$ ${}^3\text{H}$ cross section via

$$\sigma^{Cl}(E) = \frac{R_{\text{atm}}({}^6\text{Li})}{R_{\text{atm}}({}^{35}\text{Cl})} \frac{N^{Cl}(E)}{N^{Li}(E)} \sigma^{Li}(E), \quad (5)$$

where N^{Cl} and N^{Li} are the numbers of observed ${}^{35}\text{Cl}(n, p_0)$ and ${}^6\text{Li}(n, \alpha)$ ${}^3\text{H}$ reactions for a given incident neutron energy. $R_{\text{atm}}({}^6\text{Li})$ and $R_{\text{atm}}({}^{35}\text{Cl})$ are the numbers of ${}^6\text{Li}$ and ${}^{35}\text{Cl}$ atoms per CLYC molecule respectively. Values for the

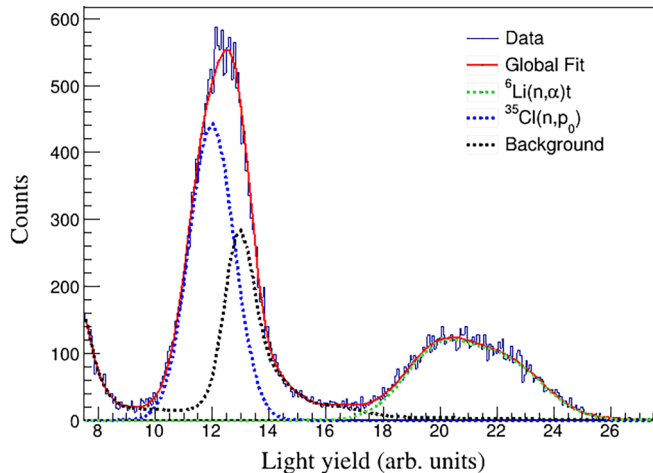


FIG. 11. Representative fit for 4.4 m data set at 2.39 MeV.

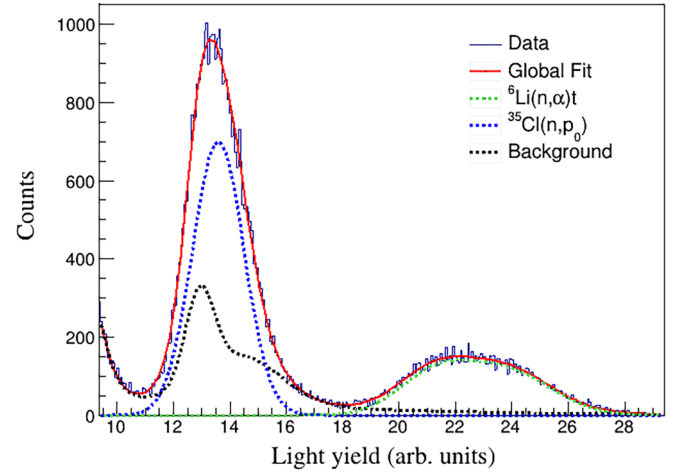


FIG. 12. Representative fit for 4.4 m data set at 2.86 MeV.

${}^6\text{Li}(n, \alpha)$ ${}^3\text{H}$ cross section were taken from the upcoming ENDF/B-VIII.1 evaluation [30]. The ENDF/B-VIII.1 evaluation was chosen over the ENDF/B-VIII.0 evaluation due to a peak in the 5–8 MeV range in the latter that does not correspond to experimental data.

The observation of the ratio requires that the bands from both reactions yield reliable estimated counts. This leads to discontinuous limited regions over which the cross section can be ascertained in this work. The accessible regions for the two flight paths are 2.02–3.49 MeV for the short flight path and 3.91–7.46 MeV for the 9.4 m long flight path. The upper limit of the long flight path is due to a lack of statistics, while the upper bound for the shorter flight path is due to clipping of the QDC. In both cases frame overlap provides a limit on the lower energy.

The accessible region was divided into ten equally sized TOF projections, this number being determined by the time resolution. For each TOF projection, a fitting model consisting of 21 parameters (with three fixed) was applied. The model consisted of a single Gaussian for the unwrapped ${}^{35}\text{Cl}(n, p_0)$ band, a sum of two Gaussians for the unwrapped

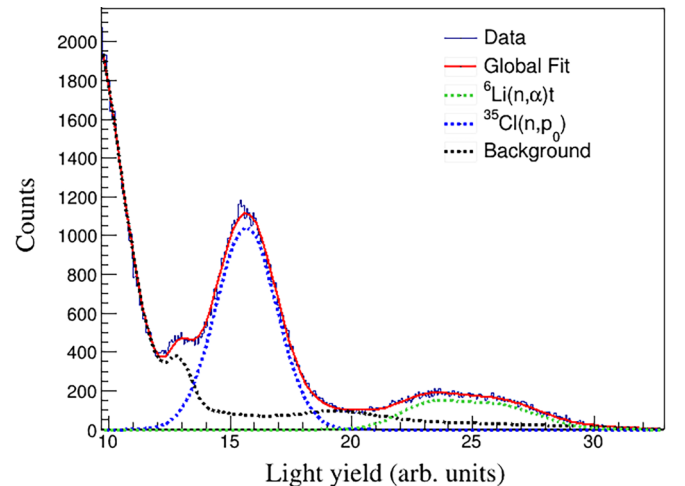


FIG. 13. Representative fit for 4.4 m data set at 3.49 MeV.

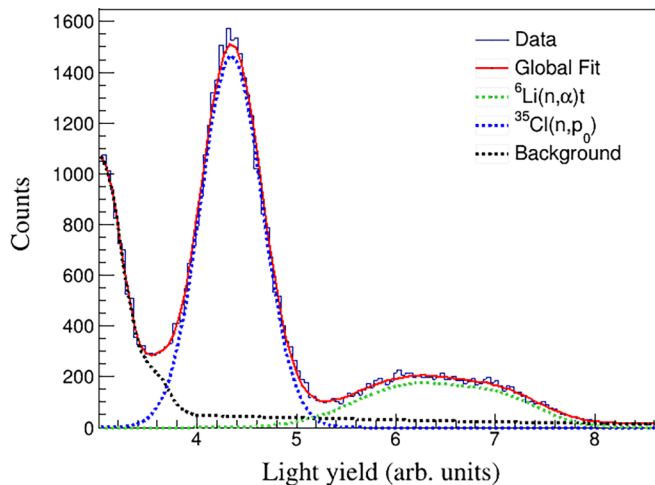


FIG. 14. Representative fit of 9.4 m data set at 3.91 MeV.

${}^6\text{Li}(n, \alpha){}^3\text{H}$ band, and an empirical background consisting of three Gaussians and a polynomial. Two Gaussians were used for the unwrapped ${}^6\text{Li}(n, \alpha){}^3\text{H}$ band due to the energy sharing between the α and triton reaction products as discussed above. The background model consisted of one Gaussian for the singly wrapped Li band, a second Gaussian for the time-independent highly-wrapped Li band, a third Gaussian to capture all other reactions [i.e., low light-producing reactions such as the ${}^{35}\text{Cl}(n, \alpha)$ and ${}^{35}\text{Cl}(n, p_i\gamma)$ and ${}^{37}\text{Cl}(n, x)$ reactions, as well as wrapped ${}^{35}\text{Cl}(n, p_0)$ bands] and a second-order polynomial to capture downscatter effects. For each TOF projection, a χ^2 minimization was performed against this model to determine the relative reaction rates of ${}^{35}\text{Cl}(n, p_0)$ with respect to ${}^6\text{Li}(n, \alpha){}^3\text{H}$ using the MINUIT2 package provided by the ROOT data analysis framework [31]. This minimization was used to obtain parameter estimates as well as uncertainties. Since the highly wrapped Li band is time independent, its parameters can be held constant during the χ^2 minimization. The three parameters for this band were obtained by performing a minimization using the full set of free parameters for a time region in which it is reasonably isolated

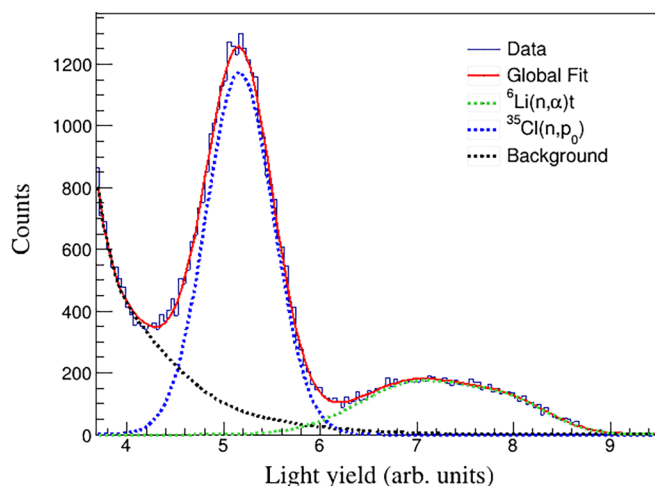


FIG. 15. Representative fit of 9.4 m data set at 4.74 MeV.

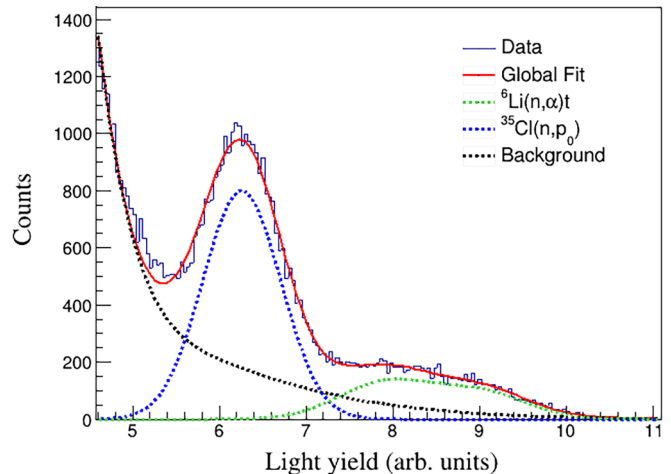


FIG. 16. Representative fit of 9.4 m data set at 5.87 MeV.

(i.e., 420 ns for 4.4 m and 360 ns for 9.4 m); these were then used as fixed parameters for the rest of the minimization. For the Gaussian consisting of “other” reactions, only the high light yield tail is used as these reactions always occur at a light yield below that of the reactions of interest. As one sweeps through TOF space, the locations and relative heights of the reaction bands change. This means that the background, while always having the same functional form, will vary dramatically with TOF. For this reason, the background parameters, with the exception of the three for the highly wrapped Li band, were allowed to vary. Four representative results from each data set are shown in Figs. 10–17.

Table I and Fig. 18 present the results using Eq. (5). The data are seen to be consistent with Kuvin *et al.* over the energy range 2.02–7.46 MeV.

D. Uncertainty quantification

Analysis parameters with inherent uncertainty in this work include the flight path length and the ${}^6\text{Li}(n, \alpha){}^3\text{H}$ cross section. Their impact on the calculated cross section is complicated due to highly correlated effects on the timing

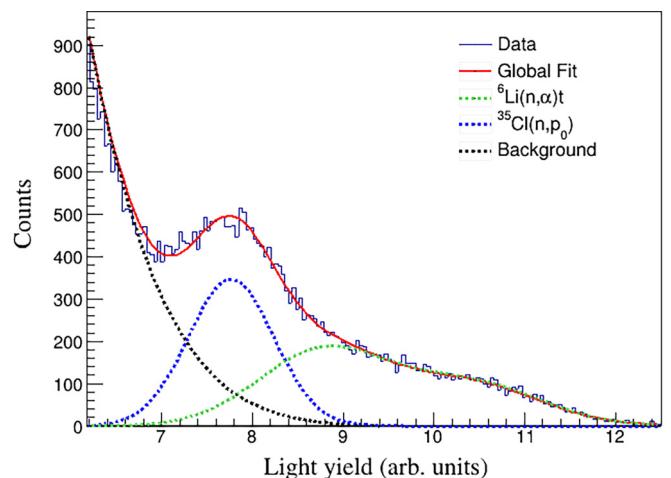


FIG. 17. Representative fit of 9.4 m data set at 7.46 MeV.

TABLE I. Angle-integrated $^{35}\text{Cl}(n, p_0)$ cross section data.

E_n (MeV)	σ (mb)	E_n (MeV)	σ (mb)
$2.02 \pm_{-0.14}^{0.16}$	61.95 ± 3.06	$3.91 \pm_{-0.13}^{0.14}$	81.77 ± 9.11
$2.14 \pm_{-0.16}^{0.17}$	57.62 ± 2.81	$4.16 \pm_{-0.15}^{0.15}$	77.85 ± 10.31
$2.26 \pm_{-0.17}^{0.19}$	58.75 ± 3.11	$4.44 \pm_{-0.16}^{0.17}$	68.32 ± 9.04
$2.39 \pm_{-0.18}^{0.21}$	63.92 ± 3.67	$4.74 \pm_{-0.18}^{0.19}$	60.76 ± 8.04
$2.53 \pm_{-0.20}^{0.23}$	67.07 ± 3.81	$5.08 \pm_{-0.20}^{0.21}$	50.82 ± 6.72
$2.69 \pm_{-0.22}^{0.25}$	77.76 ± 4.67	$5.45 \pm_{-0.22}^{0.23}$	50.06 ± 7.75
$2.86 \pm_{-0.24}^{0.27}$	71.93 ± 3.94	$5.87 \pm_{-0.24}^{0.26}$	45.29 ± 7.23
$3.05 \pm_{-0.26}^{0.30}$	78.64 ± 4.52	$6.34 \pm_{-0.27}^{0.29}$	32.70 ± 6.32
$3.26 \pm_{-0.29}^{0.33}$	79.79 ± 4.70	$6.87 \pm_{-0.31}^{0.33}$	10.72 ± 1.80
$3.49 \pm_{-0.32}^{0.37}$	94.48 ± 8.34	$7.46 \pm_{-0.35}^{0.38}$	8.94 ± 1.30

calibration, neutron energy, value of reference cross section, etc. Propagation of these uncertainties was performed via Monte Carlo, where we follow the approach given by [32]. The flight path length was randomly sampled 1000 times from a Gaussian distribution with the standard deviation set at 1 cm. For each trial, the uncertainty in the $^6\text{Li}(n, \alpha)^3\text{H}$ cross section was incorporated by multiplying the cross section uncertainty with a random number sampled from a Gaussian with a standard deviation of one. This was then added to energy window averaged cross section. Uncorrelated $^6\text{Li}(n, \alpha)^3\text{H}$ uncertainties from ENDF/B-VIII.0 were used since covariance data is not available for ENDF/B-VIII.1. For each trial, a χ^2 minimization using the MIDGRAD algorithm in the MINUIT2 minimization package provided by ROOT [31] was performed to determine the model parameter estimates and the $^{35}\text{Cl}(n, p_0)$ cross section computed. The χ^2 was used to weight the trial solutions as described by Birge [33]. Thus, the weighted mean of the 1000 trial solutions is given by

$$\bar{\sigma}^j = \frac{\sum_{i=1}^N w_i^j \sigma_i^j}{\sum_{i=1}^N w_i^j} \quad (6)$$

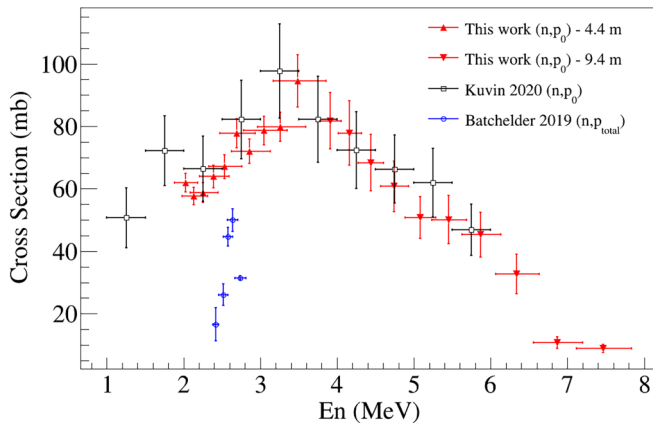


FIG. 18. Measured energy differential $^{35}\text{Cl}(n, p_0)$ cross section. The data is seen to be consistent with Kuvín *et al.* over the energy range 2.02–7.46 MeV.

where $\bar{\sigma}^j$ weighted mean of the 1000 trial solutions for TOF window j , σ_i^j is the solution for trial i for TOF window j , and w_i^j is the weighting factor for trial i and TOF window j which is given by

$$w_i = \frac{1}{\sqrt{\chi_i^2}}. \quad (7)$$

The reported cross section is the mean of this distribution. The uncertainty was determined via the standard deviation of the above distribution plus the quadrature added uncertainties from the Li and Cl abundances. The enrichment of ^6Li was assumed to be $95 \pm 1\%$ and the isotopic abundance of ^{35}Cl is 0.7576 ± 0.001 . This above distribution was also used to construct the weighted covariance matrix as given by

$$\text{cov}_{\sigma^j, \sigma^k} = \frac{\sum_{i=1}^N w_i^j w_i^k (\sigma_i^j - \bar{\sigma}^j)(\sigma_i^k - \bar{\sigma}^k)}{\sum_{i=1}^N w_i^j w_i^k}. \quad (8)$$

The covariance matrices for both data sets are provided in Appendix B.

IV. SUMMARY

Measurements of the energy-differential $^{35}\text{Cl}(n, p_0)^{35}\text{S}$ cross section from 2.02 to 7.46 MeV were conducted at the 88-Inch Cyclotron at Lawrence Berkeley National Laboratory. The experiment consisted of bombarding a CLYC scintillator with a white spectrum neutron source. Two data sets were collected: one at a short flight path length (4.4 m) and one at a long flight path length (9.4 m). For both data sets the $^{35}\text{Cl}(n, p_0)^{35}\text{S}$ cross section was determined relative to the $^6\text{Li}(n, \alpha)^3\text{H}$ reaction. These results were compared to recent measurements by Kuvín *et al.* [3] and Batchelder *et al.* [2]. The cross section obtained in this work is consistent within uncertainty with the Kuvín measurement, while the Batchelder measurement was observed to be systematically low. The reason for this is unknown at this time. It should be noted that the aforementioned results were based on a ratio of the $^{58}\text{Ni}(n, p)^{58}\text{Co}$ reaction, whose published results show considerable scatter (see Fig. 7 of [2]). A resonance in the $^{58}\text{Ni}(n, p)^{58}\text{Co}$ reaction that is not accounted for properly in the evaluated databases could be a possible reason.

ACKNOWLEDGMENTS

This work was performed under the auspices of the U.S. Department of Energy (DOE) by Lawrence Berkeley National Laboratory under Contract No. DE-AC02-05CH11231, the DOE Nuclear Energy University Program (NEUP) under Contract No. DE-NE0008992, and Lawrence Livermore National Laboratory under Contract No. DE-AC52-07NA27344. This material is based upon work supported in part by the Department of Energy National Nuclear Security Administration through the Nuclear Science and Security Consortium under Award No. DE-NA0003996. The authors thank the 88-Inch Cyclotron operations and facilities staff for their help in performing these experiments. Special thanks to Mark Paris at Los Alamos National Laboratory for providing ENDF/B-VIII.1 $^6\text{Li}(n, \alpha)^3\text{H}$ cross sections.

APPENDIX A: DAQ SETTINGS

Table II lists the DAQ parameters used in this work.

TABLE II. Summary of DAQ settings.

Parameter	CLYC-4.4 m	CLYC-9.4 m	Cyclotron RF
Record length	1472 ns	1472 ns	1472 ns
Pretrigger	288 ns	288 ns	288 ns
Polarity	Negative	Negative	Negative
Fixed baseline	15280	15280	0
DC offset	8%	8%	8%
Input dynamic range	2 Vpp	2 Vpp	2 Vpp
Threshold	300 LSB	250 LSB	100 LSB
Trigger hold-off	8496 ns	8496 ns	192 ns
Input smoothing	16 samples	16 Samples	16 samples
Energy coarse gain	160 fC/LSB/Vpp	640 fC/LSB/Vpp	40 fC/LSB/Vpp
Gate	8000 ns	8000 ns	300 ns
Short gate	148 ns	148 ns	124 ns
Pregate	108 ns	108 ns	88 ns

APPENDIX B: COVARIANCE MATRIX

Table III is the covariance matrix for the 4.4 m data set and Table IV is the covariance matrix for the 9.4 m data set.

TABLE III. Covariance matrix: 4.4 m data set.

	3.49 MeV	3.26 MeV	3.05 MeV	2.86 MeV	2.69 MeV	2.53 MeV	2.39 MeV	2.26 MeV	2.14 MeV	2.02 MeV
3.49 MeV	69.63	1.29	0.85	-1.31	-1.05	-0.54	0.37	0.43	-1.22	-0.66
3.26 MeV	1.29	22.08	0.56	0.00	0.13	-0.46	0.49	0.10	-0.15	0.52
3.05 MeV	0.85	0.56	20.45	-0.03	0.75	0.08	-0.06	-0.15	0.45	0.08
2.86 MeV	-1.31	0.00	-0.03	15.49	0.22	0.31	-0.15	0.53	0.22	-0.42
2.69 MeV	-1.05	0.13	0.75	0.22	21.78	-0.99	-1.02	-0.17	-0.52	-0.87
2.53 MeV	-0.54	-0.46	0.08	0.31	-0.99	14.52	-0.20	0.19	0.39	-0.28
2.39 MeV	0.37	0.49	-0.06	-0.15	-1.02	-0.20	13.49	0.53	-0.34	0.13
2.26 MeV	0.43	0.10	-0.15	0.53	-0.17	0.19	0.53	9.67	0.75	0.08
2.14 MeV	-1.22	-0.15	0.45	0.22	-0.52	0.39	-0.34	0.75	7.89	0.34
2.02 MeV	-0.66	0.52	0.08	-0.42	-0.87	-0.28	0.13	0.08	0.34	9.37

TABLE IV. Covariance matrix: 9.4 m data set.

	7.46 MeV	6.87 MeV	6.34 MeV	5.87 MeV	5.45 MeV	5.08 MeV	4.74 MeV	4.44 MeV	4.16 MeV	3.91 MeV
7.46 MeV	1.68	-0.13	0.24	0.60	0.16	-0.24	0.34	-0.56	0.66	-0.15
6.87 MeV	-0.13	3.23	-0.36	-0.84	1.03	0.45	-0.13	-0.29	-1.33	-0.17
6.34 MeV	0.24	-0.36	39.95	1.33	3.14	-1.29	2.61	2.76	-1.22	1.67
5.87 MeV	0.60	-0.84	1.33	52.30	-1.15	1.12	2.83	1.48	2.29	-2.52
5.45 MeV	0.16	1.03	3.14	-1.15	60.07	2.59	-0.87	1.94	-2.02	-1.69
5.08 MeV	-0.24	0.45	-1.29	1.12	2.59	45.21	3.72	-2.11	2.26	-1.89
4.74 MeV	0.34	-0.13	2.61	2.83	-0.87	3.72	64.71	3.01	0.96	-1.59
4.44 MeV	-0.56	-0.29	2.76	1.48	1.94	-2.11	3.01	81.76	3.08	-0.35
4.16 MeV	0.66	-1.33	-1.22	2.29	-2.02	2.26	0.96	3.08	106.20	-0.40
3.91 MeV	-0.15	-0.17	1.67	-2.52	-1.69	-1.89	-1.59	-0.35	-0.40	83.01

- [1] J. C. Gehin, D. E. Holcomb, G. F. Flanagan, B. W. Patton, R. L. Howard, and T. J. Harrison, *Fast Spectrum Molten Salt Reactor Options*, Technical Report ORNL/TM-2011/105 (Oak Ridge National Laboratory, Oak Ridge, TN, 2011).
- [2] J. C. Batchelder, S.-A. Chong, J. Morrell, M. A. Unzueta, P. Adams, J. D. Bauer, T. Bailey, T. A. Becker, L. A. Bernstein, M. Fratoni, A. M. Hurst, J. James, A. M. Lewis, E. F. Matthews, M. Negus, D. Rutte, K. Song, K. Van Bibber, M. Wallace, and C. S. Waltz, *Phys. Rev. C* **99**, 044612 (2019).
- [3] S. A. Kuvin, H. Y. Lee, T. Kawano, B. DiGiovine, A. Georgiadou, C. Vermeulen, M. White, L. Zavorka, and H. I. Kim, *Phys. Rev. C* **102**, 024623 (2020).
- [4] Nuclear Energy Agency, NEA nuclear data high priority request list, <https://www.oecd-nea.org/dbdata/hprl/hprlview.pl?ID=540>.
- [5] D. Brown, M. Chadwick, R. Capote, A. Kahler, A. Trkov, M. Herman, A. Sonzogni, Y. Danon, A. Carlson, M. Dunn, D. Smith, G. Hale, G. Arbanas, R. Arcilla, C. Bates, B. Beck, B. Becker, F. Brown, R. Casperson, J. Conlin *et al.*, *Nucl. Data Sheets* **148**, 1 (2018).
- [6] M. Martin, M. Auferio, E. Greenspan, and M. Fratoni, *Trans. Am. Nucl. Soc.* **116**, 1174 (2017).
- [7] J. N. Warren, $^{35}\text{Cl}(n, p)$ reactions in a ^6Li enhanced CLYC detector, Master's thesis, Ohio University, 2021.
- [8] M. Ayllon, P. A. Adams, J. C. Batchelder, J. D. Bauer, T. A. Becker, L. A. Bernstein, S.-A. Chong, J. James, L. E. Kirsch, K.-N. Leung, E. F. Matthews, J. T. Morrell, P. R. Renne, A. M. Rogers, D. Rutte, A. S. Voyles, K. Van Bibber, and C. S. Waltz, *Nucl. Instrum. Methods Phys. Res. Sect. A* **903**, 193 (2018).
- [9] P. W. Lisowski and K. F. Schoenberg, in *Proceedings of the 7th International Conference on Accelerator Applications* [*Nucl. Instrum. Methods Phys. Res., Sect. A* **562**, 910 (2006)].
- [10] P. E. Koehler, *Phys. Rev. C* **44**, 1675 (1991).
- [11] Y. P. Popov and F. L. Shapiro, *Sov. J. Nucl. Phys.* **13**, 1132 (1961).
- [12] N. D'Olympia, P. Chowdhury, C. Lister, J. Glodo, R. Hawrami, K. Shah, and U. Shirwadkar, *Nucl. Instrum. Methods Phys. Res. Sect. A* **714**, 121 (2013).
- [13] N. D'Olympia, P. Chowdhury, E. Jackson, and C. Lister, *Nucl. Instrum. Methods Phys. Res. Sect. A* **763**, 433 (2014).
- [14] L. E. Kirsch, M. Devlin, S. Mosby, and J. Gomez, *Nucl. Instrum. Methods Phys. Res. Sect. A* **874**, 57 (2017).
- [15] T. Martinez, A. Perez de Rada, D. Cano-Ott, R. Santorelli, I. Bandac, P. Garcia Abia, A. Garcia, A. Ianni, E. Mendoza, B. Montes, L. Romero, and D. Villamarin, *Nucl. Instrum. Methods Phys. Res. Sect. A* **906**, 150 (2018).
- [16] M. B. Smith, T. Achtzehn, H. R. Andrews, E. T. H. Clifford, H. Ing, and V. D. Kovaltchouk, *IEEE Trans. Nucl. Sci.* **60**, 855 (2013).
- [17] M. Kireeff Covo, R. Albright, B. Ninemire, M. Johnson, A. Hodgkinson, T. Loew, J. Benitez, D. Todd, D. Xie, T. Perry, L. Phair, L. Bernstein, J. Bevins, J. Brown, B. Goldblum, M. Harasty, K. Harrig, T. Laplace, E. Matthews, A. Bushmaker, D. Walker, V. Oklejas, A. Hopkins, D. Bleuel, J. Chen, and S. Cronin, *Measurement* **127**, 580 (2018).
- [18] CLYC Gamma-Neutron Scintillator, Radiation Monitoring Devices, 2024.
- [19] H13795-100 (R13435-100 Hybrid Assembly), Hamamatsu Photonics, 2018.
- [20] Silicone Rubber Optical Interface EJ-560, Eljen Technology, 2021.
- [21] 902CG Self-Leveling 360-Degree Cross Line Laser Level with Pulse Mode and Magnetic Pivoting Base, 2024, <https://uk.huepar.com/products/huepar-902cg-self-leveling-360-degree-cross-line-laser-level-with-pulse-mode-switchable-horizontal-and-vertical-green-beam-laser-tool-magnetic-pivoting-base-included>.
- [22] J. T. Morrell, A. S. Voyles, J. C. Batchelder, J. A. Brown, and L. A. Bernstein, *Phys. Rev. C* **108**, 024616 (2023).
- [23] K. Harrig, B. Goldblum, J. Brown, D. Bleuel, L. Bernstein, J. Bevins, M. Harasty, T. Laplace, and E. Matthews, *Nucl. Instrum. Methods Phys. Res. Sect. A* **877**, 359 (2018).
- [24] DT5730/DT5725: 8 Channel 14-bit 500/250 MS/s Digitizer, CAEN Technologies, 2023, <https://www.caen.it/products/dt5725/>.
- [25] 725 and 730 DPP-PSD: Register Description and Format, CAEN Technologies, 2023, <https://www.caen.it/products/dpp-psd/>.
- [26] CoMPASS: Multiparametric DAQ Software for Physics Applications, CAEN Technologies, 2023, <https://www.caen.it/products/compass/>.
- [27] P. Prusachenko and T. Bobrovskiy, *Nucl. Instrum. Methods Phys. Res., Sect. A* **1056**, 168582 (2023).
- [28] S. Agostinelli, J. Allison, K. Amako, J. Apostolakis, H. Araujo, P. Arce, M. Asai, D. Axen, S. Banerjee, G. Barrand *et al.*, *Nucl. Instrum. Methods Phys. Res. Sect. A* **506**, 250 (2003).
- [29] J. B. Birks, *The Theory and Practice of Scintillation Counting* (Pergamon, London, 1964).
- [30] M. Paris (private communication).
- [31] R. Brun and F. Rademakers, *Nucl. Instrum. Methods Phys. Res. Sect. A* **389**, 81 (1997).
- [32] D. Smith and N. Otuka, *Nucl. Data Sheets* **113**, 3006 (2012).
- [33] R. T. Birge, *Phys. Rev.* **40**, 207 (1932).